Effect of Radial Location of Nozzles on Heat Transfer in Preswirl Cooling Systems

V. U. Kakade
G. D. Lock
M. Wilson
J. M. Owen
J. E. Mayhew[1]

Department of Mechanical Engineering,
University of Bath,
Bath BA2 7AY, U.K

This paper investigates heat transfer in a rotating disk system using preswirled cooling air from nozzles at high and low radius. The experiments were conducted over a range of rotational speeds, flow rates, and preswirl ratios. Narrow-band thermochromic liquid crystal (TLC) was specifically calibrated for application to experiments on a disk, rotating at ~5000 rpm and subsequently used to measure surface temperature in a transient experiment. The TLC was viewed through the transparent polycarbonate disk using a digital video camera and strobe light synchronized to the disk frequency. The convective heat transfer coefficient h was subsequently calculated from the one-dimensional solution of Fourier's conduction equation for a semi-infinite wall. The analysis was accounted for the exponential rise in the air temperature driving the heat transfer, and for the experimental uncertainties in the measured values of h. The experimental data was supported by "flow visualization," determined from CFD. Two heat transfer regimes were revealed for the low-radius preswirl system: a viscous regime at relatively low coolant flow rates, and an inertial regime at higher flow rates. Both regimes featured regions of high heat transfer where thin, boundary layers replaced air exiting through receiver holes at high radius on the rotating disk. The heat transfer in the high-radius preswirl system was shown to be dominated by impingement under the flow conditions tested.
[DOI: 10.1115/1.4001189]

1 Introduction

In gas turbines, air is diverted from the compressor to the turbine through a system of channels, pipes, and sealed cavities. The main purpose of this secondary air system is to prevent hot-gas ingestion and supply cooling air, at the lowest possible temperature, to the turbine components. In a high-pressure turbine stage, this cooling air is expanded through stationary, angled preswirl nozzles, transferred through a wheel-space, and delivered to blade receiver holes on the rotating disk. The nozzles swirl the air, and this reduces the work done by the rotating turbine disk in accelerating the air to the disk speed; this consequently reduces the relative total temperature of the air entering the receiver holes, which guide the coolant to the rotor-blade roots.

Scricca and Moore [1] discussed a diverse range of preswirl designs. For a given rim-cavity pressure, disk speed, coolant delivery temperature and pressure, and receiver hole radius, the performance of a preswirl system may be quantified by the mass flow rate and temperature of the coolant delivered through the receiver holes. This performance depends on factors such as: nozzle and receiver hole discharge coefficients, leakage and mixing losses, rotating disk windage, rotating-cavity geometry, and heat transfer between the preswirl air and the disk.

A simplified diagram of a preswirl system is shown in Fig. 1(*a*), where the radius of the nozzles is shown to be lower than that of the receiver holes; this is termed as a *low-radius preswirl system*. In an alternative design, these radii might be equal, and this is termed as a *high-radius preswirl system*. The low-radius design can have the advantage of reduced leakage losses. El-Oun and Owen [2] were the first to produce a theoretical model of adiabatic effectiveness. Chew et al. [3] and Farzaneh-Gord et al. [4] also independently derived theoretical models of effectiveness, showing that a high-radius design can supply lower cooling air temperatures. The optimum configuration depends upon the engine-designer's goal: If the minimum coolant temperature is the primary goal, then a high-radius design is preferable (e.g., military aero-engines); keeping the preswirler exit pressure as low as possible minimizes leakage, which improves turbine efficiency, and if this is the primary goal (e.g., civil aero-engines), then a low-radius design is preferable. Consideration must also be given to balancing the load on the thrust bearing [1].

Preswirl research has been widely published at ASME conferences. Meierhofer and Franklin [5] were the first to experimentally confirm the significant reduction in a relative total temperature using a preswirl system, and quantified the effectiveness of such a system in terms of the ratio of delivery air velocity to disk speed. El-Oun and Owen developed a simple model, based on the Reynolds analogy for an adiabatic system to predict the adiabatic effectiveness. The predictions, which were in good agreement with the experiment, showed that the effectiveness increased monotonically as the preswirl ratio increased. Wilson et al. [6] used total-temperature probes to measure the temperature of the air entering receiver holes, which was consistently underpredicted by axisymmetric computations. Geis et al. [7] measured the total temperature of the air entering the receiver holes, which were significantly higher than the values predicted from their ideal model. Chew et al. published numerical simulations that were in good agreement with results from both the Karlsruhe preswirl rig used by Geis et al. and a preswirl rig at Sussex University. Dittmann et al. [8] measured the discharge coefficients for preswirl nozzles and receiver holes, including holes with radiused and chamfered inlets [9]. Yan et al. [9] measured, and Lewis et al. [10] computed, the discharge coefficient of receiver holes, showing that they reached a maximum when the rotating core of fluid was in synchronous rotation with the holes.

Yan et al. and Lewis et al. studied a low-radius system, while the Karlsruhe rig, used by Dittman et al. [11,8], featured preswirl nozzles and receiver holes at the same radius. Jarzombek et al. [12] studied computationally a configuration with the preswirl nozzles located radially outward of the receiver holes. Lewis et al.

[1]Present address: Rose–Hulman Institute of Technology, IN.

Contributed by the International Gas Turbine Institute (IGTI) of ASME for publication in the JOURNAL OF TURBOMACHINERY. Manuscript received July 27, 2009; final manuscript received August 5, 2009; published online October 26, 2010. Editor: David Wisler.

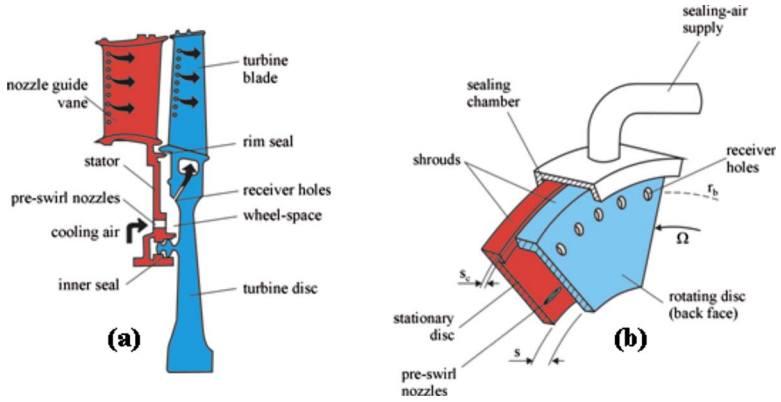

Fig. 1 (*a*) Typical gas turbine rotor-stator system with preswirled cooling air; (*b*) simplified model

[13] investigated, computationally, the effect of the radial location of the preswirl nozzles, concluding that the variation in static pressure in the core will reduce, but not negate, the advantages of locating the preswirl nozzles at a radius as high as practicable. It was also shown that the increase in effectiveness with increased preswirl-nozzle radius is caused solely by losses in the nozzles and in the core.

The engine designer is interested in calculating the pressure drop and cooling effectiveness of the preswirl system, but there is also a need to understand the heat transfer between the cooling air and the turbine disk. Lock et al. [14] measured the local Nusselt number, Nu, on the rotating disk in the low-radius preswirl system used by Yan et al. [9] and Lewis et al. [10,13]. The experiments were conducted over a range of rotational speeds, flow rates, and preswirl ratios, and showed that Nu was virtually axisymmetric, except near the receiver holes, where large variations occurred.

This paper explores the effect of the radial location of the preswirl nozzles on the heat transfer between the air and the rotating disk. The experimental facility is a simplified model of a gas turbine rotor-stator system designed to accommodate pressure and temperature instrumentation in the test section, and to provide optical access to the wheel-space.

2 Experimental Facility

Owen and Rogers [15] showed that, for a rotating cavity, the turbulent flow structure is principally governed by two nondimensional parameters: the inlet swirl ratio β_p, and the turbulent flow parameter λ_T. These are defined as

$$\beta_p = \frac{V_{\phi,p}}{\Omega r_p} \tag{2.1}$$

and

$$\lambda_T = c_w \, \mathrm{Re}_\phi^{-0.8} \quad \text{where} \quad c_w = \frac{\dot{m}_p}{\mu b} \tag{2.2}$$

and

$$\mathrm{Re}_\phi = \frac{\rho \Omega b^2}{\mu} \tag{2.3}$$

The value $\lambda_T = 0.22$ corresponds to the flow rate entrained by a disk rotating in an infinite environment, which is the so-called free disk. The heat transfer depends upon the flow structure and also the rotational Reynolds number Re_ϕ.

The experimental facility uses a simplified model of a gas turbine rotor-stator system, designed to accommodate pressure and temperature instrumentation in the test section and to provide optical access to the wheel-space. Experiments were conducted at engine-representative values of β_p and λ_T, thereby producing flow structures typical of those found in a gas turbine. In engines, Re_ϕ is of the order of 10^7, which is an order-of-magnitude greater than that achievable in the rig. As the heat transfer depends strongly on Re_ϕ, as well as on β_p and λ_T, the rig Nusselt numbers will be much smaller than those found in engines. This is discussed further in Sec. 5.

The geometry, which was based on information obtained for existing engine designs, is illustrated schematically in Fig. 1(*b*). Air entered the test section through the stator via preswirl nozzles and exited through 60 axial receiver holes in the disk representing the entrance to blade-cooling passages in the engine. Both low-radius and high-radius preswirl designs were used, with $r_p/r_b = 0.8\pm$ and 1.0, respectively. Both designs used 24 cylindrical holes as preswirl nozzles. The geometric properties of the test rig and the range of operating conditions are summarized in Table 1.

3 Experimental Technique

The use of thermochromic liquid crystal (TLC) in heat transfer experiments is a well-established practice; Ireland and Jones [16] and Baughn [17] provide reviews of how the technology has been utilized in a range of fluid-flow applications. In a transient experiment, each site on the TLC surface will change color through the optically active temperature range, and this process is captured digitally. If the time at which the TLC changes color is known (so that the surface temperature is also known), then the heat transfer coefficient h can be calculated from the one-dimensional solution of Fourier's conduction equation for a semi-infinite wall.

Local heat transfer coefficients on the rotating disk were determined from transient surface temperature measurements using two calibrated narrow-band TLCs (designated as 30°C and 40°C to indicate their activation temperatures). The experiments were conducted under known thermal boundary conditions, using air, which had been preheated to approximately 50°C using a mesh heater (see Ref. [18]) upstream of the preswirl nozzles. The crystals were sprayed on the disk in sectors inside the wheel-space, which could be viewed through the transparent polycarbonate by a digital video camera.

Table 1 Summary of geometry and operating conditions

Disk outer radius (b)	216 mm
Inner radius (a)	$a/b = 0.67$
Gap ratio	$s/b = 0.051$
Low preswirl radius (r_p)	$r_p/b = 0.74$
High preswirl radius (r_p)	$r_p/b = 0.93$
Receiver-hole radius (r_b)	$r_b/b = 0.93$
Re_ϕ	0.8×10^6–1.2×10^6
λ_T	0.12–0.36
β_p	0.4–1.8

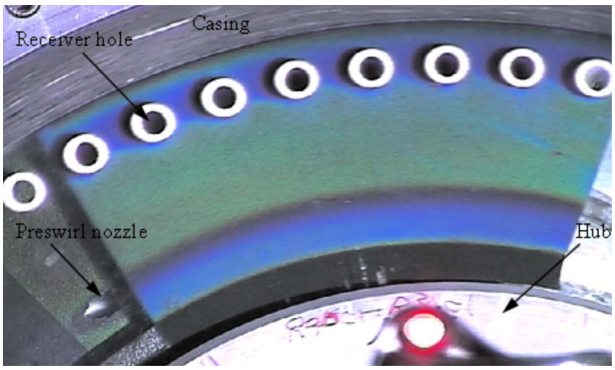

Fig. 2 Photograph of TLC on disk rotating at 5000 rpm ($Re_\phi = 1\times10^6$, $\lambda_T = 0.12$)

Figure 2 is a color image selected from a time sequence during a typical experiment using the low-radius preswirl geometry. This image shows the activated TLC as viewed through the transparent polycarbonate disk, rotating clockwise in this view. Initially clear when below its activation temperature, the TLC changed color from red to green to blue as the disk was heated by the hot air entering through the preswirl nozzles. The image appears "frozen" because the rotor was illuminated by stroboscopic light synchronized with the disk rotating at 5000 rpm. The hub, casing (at radii a and b), and blade receiver holes (insulated using low-conductivity, white Rohacell foam) are labeled in the figure. The TLC and overcoat of black paint had been sprayed in a 48 deg sector on the disk covering eight of the 60 receiver holes. To the left of this painted sector on the rotor, the stator (coated with wide-band TLC) and two of the preswirl nozzles are visible through the transparent (unpainted) polycarbonate at low radius. Some shadows appear around the receiver holes due to constraints with the lighting and viewing angles. Both the 30°C and 40°C TLCs have been activated into their visible range, and displayed different colors at different locations on the rotating disk. Blue indicates higher temperature, revealing that there is a region of relatively high heat transfer around the receiver holes; the virtually identical color patterns around each of these holes illustrate circumferential periodicity of the flow structure. Color images, recorded by a digital video camera running at 25 frames per second, were subsequently converted to hue. As explained in Sec. 4, it was then possible to determine a hue-time pair at each measurement point on the disk.

A typical example of the variation in the measured total-temperature with the time of the preswirl cooling air is shown in Fig. 3. The air temperatures were measured using a fast-response total-temperature probe, carefully calibrated for recovery factor. The measurements were made at two locations: The first location is immediately downstream of the mesh heater, and here, the temperature can be seen to exhibit a virtual step-change from an initial value of around 20°C to a final steady-state temperature ≈53°C; the second location is at the exit of the preswirl nozzles, where the air enters the test section. Despite the thermal insulation in the upstream pipes, the air temperature at this latter location rises exponentially from its initial value toward a final steady-state temperature. A three-term exponential fit was used and the total-temperature T_a history at the preswirl nozzles (Fig. 3) can be represented by the following:

$$T_a = 23.5 + 7.3(1 - e^{-t/7.9}) + 6.0(1 - e^{-t/0.9}) + 16.1(1 - e^{-t/0.05}) \tag{3.1}$$

Typically, the crystal color-change times on the disk surface ranged between 1 s and 45 s (depending on the local heat flux), and these times can be of similar magnitude to the time constants of the exponential rise in gas temperature.

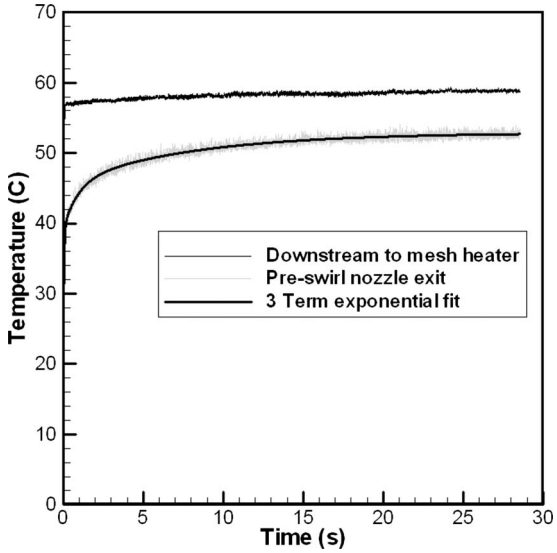

Fig. 3 Typical variation in air temperature with time

4 Data Analysis

The heat transfer coefficient h is defined as

$$q_w = h(T_{\text{aw}} - T_w) \tag{4.1}$$

where q_w is the surface heat flux from the air to the wall, T_w is the surface temperature of the wall, and T_{aw} is the adiabatic-wall temperature. T_{aw} depends on the total-temperature of the air T_a and on the fluid dynamics. The method of analysis to determine h for the transient heat transfer experiments is based on the solution of Fourier's one-dimensional conduction equation for a semi-infinite substrate, as described by Newton et al. [18]. The one-dimensional analysis considers only the conduction in the direction normal to the surface of the wall, ignoring conduction in the transverse directions. Kingsley-Rowe et al. [19] provided an analytical correction where lateral conduction is significant.

The general solution to Fourier's equation for an exponential series in air-driving temperature, corresponding, for the case of $m=3$ terms, to Eq. (3.1), is given by Newton et al. as

$$\Theta = \frac{T_w - T_0}{T_{\text{aw},\infty} - T_0} = \sum_{j=1}^{m} \frac{T_{a,j}}{T_{\text{aw},\infty} - T_0} g(\beta, \beta_{\tau_j}) \tag{4.2}$$

where

$$g(\beta, \beta_\tau) = 1 - \frac{1}{1+\beta_\tau^2} e^{\beta^2} erfc(\beta) - e^{-t/\tau} \frac{\beta_\tau^2}{1+\beta_\tau^2} \xi \tag{4.3}$$

$$\xi = \left\{ 1 + \frac{1}{\beta_\tau} \left[\frac{1}{\pi} \sqrt{\frac{t}{\tau}} + \frac{2}{\pi} \sum_{n=1}^{\infty} \frac{1}{n} e^{-n^2/4} \sinh\left(n \sqrt{\frac{t}{\tau}} \right) \right] \right\} \tag{4.4}$$

$$\beta = \frac{h\sqrt{t}}{\sqrt{\rho c k}} \quad \text{and} \quad \beta_\tau = \frac{h\sqrt{\tau}}{\sqrt{\rho c k}} \tag{4.5}$$

A method of quantifying and minimizing measurement uncertainties is described by Owen et al. [20]. Small uncertainties in the measured temperatures can create large uncertainties in the calculated value of h, and the amplification parameter Φ_h^* is defined as the ratio of the relative uncertainty in h to the relative uncertainties in the temperatures. The minimum value of Φ_h^* occurs for $\Theta \approx 0.5$ (though the variation is relatively small for $0.4 < \Theta < 0.6$), and ideally, this is the range of Θ, in which experiments with a single TLC should be conducted if the uncertainties in h are to be kept to a minimum. Owen et al. also show that it is advan-

Table 2 Summary of parameters relevant to data shown in Fig. 4, using a single-point calibration at $H=0.53$ for both the 30°C and 40°C crystal. The uncertainty in the wall temperature is $P_T=0.2$ C, $T_0=23.5$ C, and $T_{aw,\infty}=52.9$ C.

TLC	T_w	time (s)	Θ	λ_1	λ_2	λ_3	β	$\beta_{\tau 1}$	$\beta_{\tau 2}$	$\beta_{\tau 3}$	h (W/m^2 K)	Φ_h^*	P_h (W/m^2 K)
30°C	31.4	3.04	0.27	0.62	1.83	8.05	0.42	0.68	0.23	0.05	135	8.7	7.9
40°C	41.2	23.0	0.6	1.71	5.02	22.1	1.18	0.68	0.23	0.05	138	5.5	5.1

tageous to design an experiment where τ is as small as practicable. Typical values of Θ, $\lambda=\beta/\beta_\tau=\sqrt{t/\tau}$, β_τ, and Φ_h^* for the experiments with the two crystals are given below in Table 2.

The experimental application uses the 30°C and 40°C crystals to identify two particular isotherms (each at a particular calibrated hue, H) on the test surface at two measured times in the transient experiment. Over the narrow calibrated-temperature range that the crystals are active (~1°C), a unique value of hue is used for the single-point measurement of the wall temperature. The experiment begins with the disk at a known initial temperature, below the activation temperature of both crystals. During the transient process, the color changes of the crystals were recorded as the disk was heated convectively. The data were subsequently converted into a series of frames (25 per second) and stored as bitmap using the software AVID LIQUID 7.0 in a completely automated manner. Three receiver holes on the disk surface fit into a camera-image area of 450×450 pixels. A median filter is used in each 10×10 pixels area within the image to determine the hue history at each pixel.

Figure 4 shows a typical hue history measured at one location, where the scales of the lower and upper abscissa, measured in frames, as well as the left and right ordinates, (measured in hue) differ for the two crystals. The 30°C and 40°C crystals are seen to be active between (approximately) frames 50–100 and 460–700, respectively. Though h is invariant with time, the heat flux at any location decreases with time as the difference between the wall and gas-driving temperature decreases. The rate of increase in hue is correspondingly greater for the 30°C crystal.

The value of the hue for the single-point calibration of both crystals has been chosen as $H=0.53$. The time at which this value of H is reached was calculated from the smoothed H-time data, using a range of ten frames on either side of the *reference frame*, at which $H\approx0.53$. A low-pass digital filter and cubic-spline interpolation (marked in the figure) were used for this purpose. In this way, the uncertainty in time was reduced to an insignificant value ($\ll$40 ms).

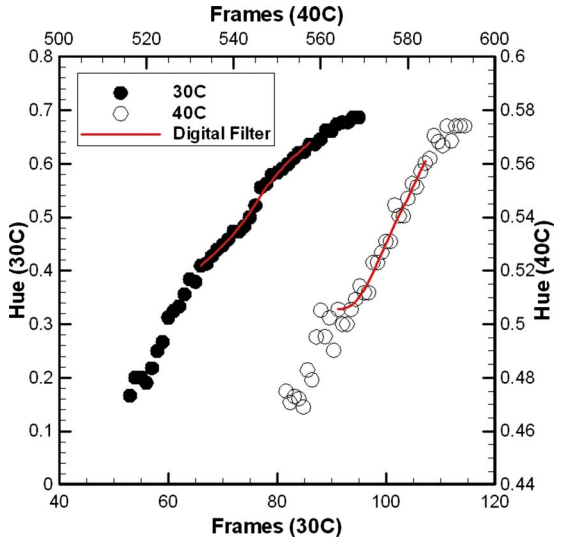

Fig. 4 Variation in hue during transient experiment

The air temperature history for the data in Fig. 4 is shown in Fig. 3, and the three-series exponential fit is given by Eq. (3.1). Table 2 lists the relevant nondimensional parameters in the solution of Fourier's equation for the data at this pixel. It is noted that the values of Θ, λ, and β_τ are sufficiently advantageous to result in acceptable values of Φ_h^* and the uncertainties of P_h for both crystals. Also, the difference between these two values of h, assumed invariant with time, is smaller than the theoretical uncertainties of the measurements.

The choice of H for the single-point calibration was arbitrary. The value of h, determined from the data in Fig. 4 for any value of hue over the range $0.3<H<0.6$, was equal within experimental uncertainty, listed as P_h in Table 2.

5 Experimental Results

Experimental data has been collected over a range of preswirl mass flow rates, swirl ratios, and rotational Reynolds numbers for both the low- and high-radius preswirl systems. Five cases, shown in Table 3, will be discussed in detail.

5.1 Low-Radius Preswirl System. For the low-radius preswirl system, two heat transfer regimes were observed: a *viscous* regime at relatively low values of λ_T and an *inertial* regime at high values of λ_T. Cases 1 and 2 fit into the latter and former regimes, respectively. The viscous regime corresponds to the axisymmetric boundary layer flow over most of the rotating disk. The inertial regime features an impingement on the disk near the preswirl-nozzle radius with an associated peak in h.

Figure 5(a) shows a contour map of the heat transfer coefficient on the rotating disk in the circumferential section for Case 1. No data is shown in the immediate vicinity of the receiver holes as these were insulated using the Rohacell foam—see Fig. 2. The disk is shown rotating in the clockwise direction, and the data is determined from the 40°C narrow-band TLC. The fluid-dynamic conditions feature a relatively high value of λ_T, hence, relatively high-velocity jets exiting the preswirl nozzles; this inertial-flow regime is dominated by impingement on the rotating disk. There is a strong radial variation in h, with the highest levels located at the nozzle radius. High levels of h are also measured adjacent to the receiver holes where the three-dimensional flow near the surface of the disk creates a nonaxisymmetric distribution of h. The virtually identical contour patterns around each of the three receiver holes indicate the circumferential periodicity of the flow structure.

Superimposed onto Fig. 5(a) are streamlines relative to the rotor calculated from the CFD code, CFX [10]. These streamlines are

Table 3 Five experimental cases

Case	λ_T	β_p	β_∞	r_p/r_b	Re_φ
1	0.35	1.5	0.65	0.8	1×10^6
2	0.12	0.5	0.3	0.8	1×10^6
3	0.36	1.2	1.0	1	1×10^6
4	0.12	0.4	0.4	1	1×10^6
5	0.28	1.8	1.3	1	0.8×10^6

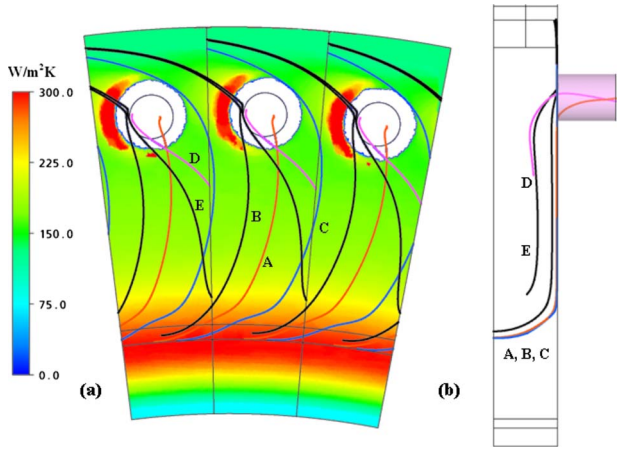

Fig. 5 (*a*) Heat transfer coefficient in circumferential section; (*b*) computed streamlines in radial section—Case 1

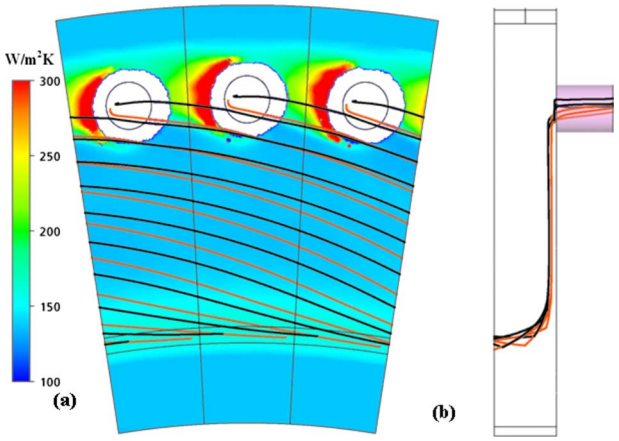

Fig. 6 (*a*) Heat transfer coefficient in circumferential section; (*b*) computed streamlines in radial section—Case 2

used as supporting flow visualization information, and are also shown in the radial section in Fig. 5(*b*) (with the preswirl inlet and stator on the left, and the receiver hole and rotor on the right.)

Wilson et al. [6] conducted a computational study, which showed that air entered the receiver holes by *direct* and *indirect* routes. The former refers to the flow traveling directly along a streamline, connecting the inlet and the outlet, and therefore, not mixing with the core flow. Indirect flow mixes with the core flow before entering the receiver holes.

Streamline A (orange) is an example of a direct streamline; it enters the wheel-space through the preswirl nozzles and is entrained into the disk boundary layer, continues to a higher radius, and then flows out through the receiver hole. Streamline B (black) impinges onto the downstream side of the hole, forming part of a new boundary layer, then continues to a higher radius where it will recirculate into the system and mix with the core flow; this impingement and the associated thin boundary layer gives rise to the crescent-shaped region of high heat transfer on the downstream side of each receiver hole.

Streamline C (blue), like streamline B, also forms part of the indirect flow, which mixes with the core flow; unlike B, this streamline is entrained into a flow, which passes between two receiver holes, and the associated thicker boundary layer creates a relatively low heat transfer coefficient.

The two indirect streamlines (D and E) show that the flow, which has entered the core, can either exit through the receiver hole (D, pink) or continue circulating in the core (E, black). The latter flow, again by impingement and the thin boundary layer associated with the replacement of the boundary layer flow entering the receiver holes, contributes to the region of high heat transfer on the downstream side of each hole.

Figure 6(*a*) is a contour map of heat transfer coefficient on the rotating disk in the circumferential section for Case 2, where fluid-dynamic conditions feature a relatively low value of λ_T. Here, there is relatively weak impingement from the preswirl nozzles and this viscous-flow regime is dominated by the boundary layer on the rotating disk. The largest levels of h are measured near the receiver holes where the three-dimensional flow near the surface of the disk again creates a nonaxisymmetric distribution of h. Superimposed onto the contours are two streamlines of cooling air from the preswirl nozzles; these are also shown in the radial section in Fig. 6(*b*). The orange streamline is entrained into the disk boundary layer, continues to a higher radius, and then flows directly out through the receiver hole. The black streamline has a less direct route, impinging onto the downstream side of the hole and forming part of a new boundary layer, eventually exiting through the next (anticlockwise) receiver hole; this impingement and the associated thin boundary layer gives rise to the crescent-shaped region of high heat transfer on the downstream side of each receiver hole.

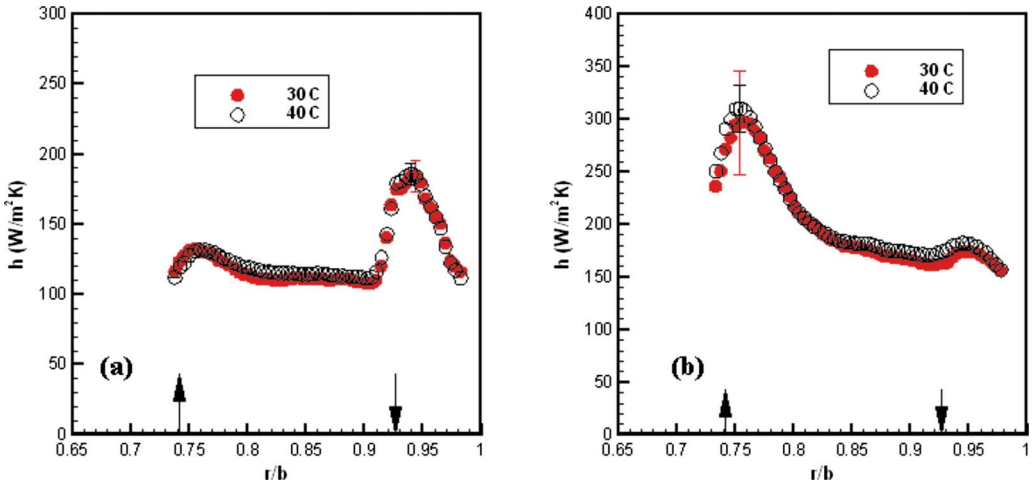

Fig. 7 Radial variation in heat transfer coefficient determined by 30°C and 40°C crystals: (*a*) Case 2 and (*b*) Case 1

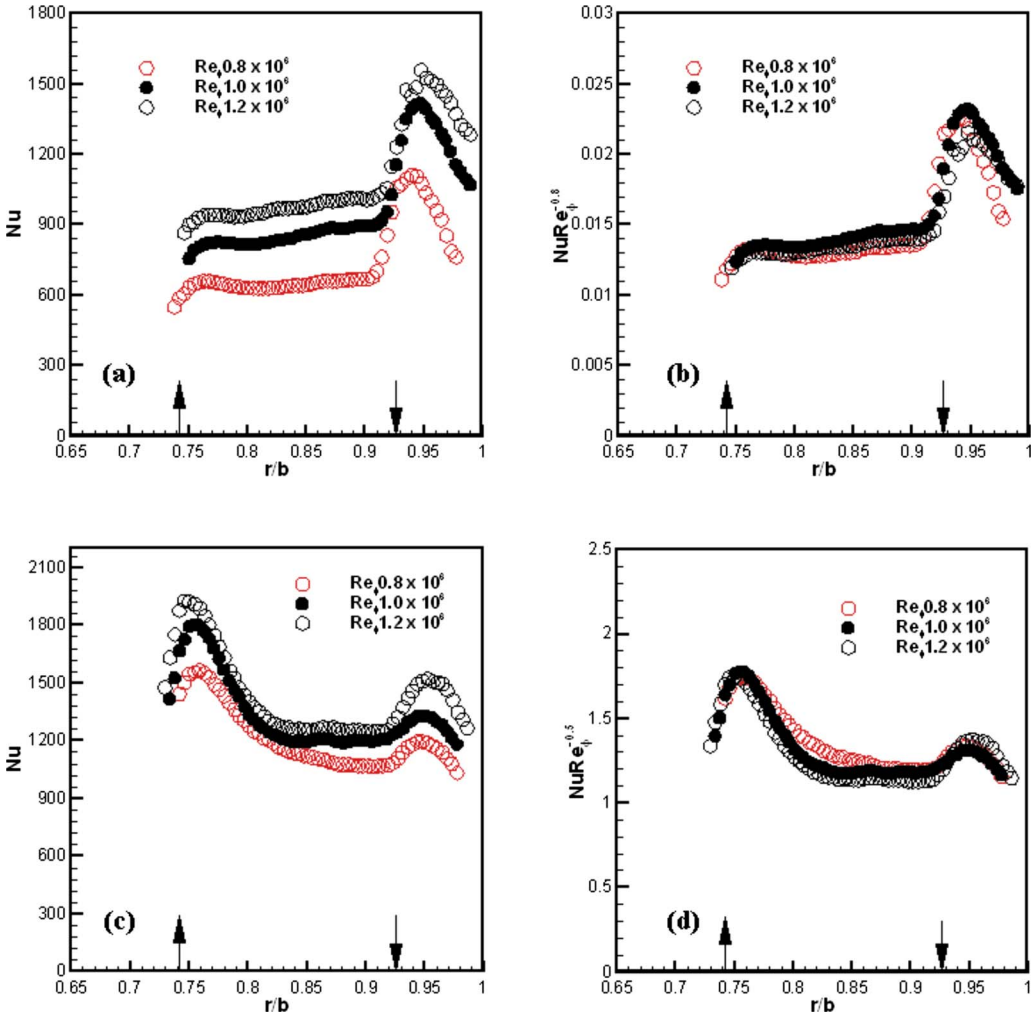

Fig. 8 Viscous regime (*a*) radial variation in Nu; (*b*) radial variation in Nu $Re_\phi^{-0.8}$; inertial regime (*c*) radial variation in Nu; (*d*) radial variation in Nu $Re_\phi^{-0.5}$

Figures 7(*a*) and 7(*b*) show the variation in h, determined using both the 30°C and 40°C crystals, with nondimensional radius (r/b) along a line midway between two receiver holes for Cases 1 and 2. The preswirl inlet and receiver hole exit locations are marked by arrows in the figures. The close agreement between the two data sets determined by the exponential series solution illustrates the accuracy of the experiments and validates the calibration and method of analysis. The maximum uncertainties, as determined by the method of Owen et al. [20], are also shown in these figures. A similarly close agreement occurred for all the cases considered.

The local Nusselt number is defined as

$$\mathrm{Nu} = \frac{hr}{k} \tag{5.1}$$

Figure 8(*a*) illustrates the effect of Re_ϕ on the radial variation in Nu for a fixed value of $\lambda_T = 0.12$ (for which $\beta_p = 0.5$), corresponding to the viscous regime. The magnitude of Nu increases with increasing Re_ϕ at all radii, but there is little effect of Re_ϕ on the *shape* of the Nu distribution. Owen and Rogers [15] showed that, for the turbulent boundary layer flow in rotor-stator systems, $\mathrm{Nu} \propto \mathrm{Re}_\phi^{0.8}$. Figure 8(*b*) shows that the parameter $\mathrm{Nu}\,\mathrm{Re}_\phi^{-0.8}$ is virtually independent of Re_ϕ for $0.73 < r/b < 0.9$, suggesting that the heat transfer for the viscous regime is controlled by the turbulent boundary layer flow. The parameter fails to collapse the data near the receiver holes $(r/b > 0.9)$, where other fluid-dynamic effects dominate.

Figure 8(*c*) illustrates the effect of Re_ϕ on the radial variation in Nu for a fixed value of $\lambda_T = 0.35$ (for which $\beta_p = 1.5$), corresponding to the inertial regime. Again the magnitude of Nu increases with increasing Re_ϕ, and again, there is little effect of Re_ϕ on the shape of the Nu distribution. Fang et al. [21] showed that, for impingement onto a rotating disk, $\mathrm{Nu} \propto \mathrm{Re}_\phi^{0.4}$. Opposite the preswirl nozzles, the best correlating parameter for the data in Fig. 8(*c*) was $\mathrm{Nu}\,\mathrm{Re}_\phi^{-0.5}$, indicating that the heat transfer for the inertial regime is governed by impingement. This parameter also collapses the data in the vicinity of the receiver holes, suggesting that impingement effects are important in this region.

5.2 High-Radius Preswirl System. For the low-radius system, experimental results were only possible with preswirl ratios below the critical ratio for synchronous rotation of the core and disk at the receiver hole radius, i.e. $\beta_\infty = V_{\phi,\infty}/\Omega r_b = 1$. Using the high-radius preswirl system it was possible to create synchronous rotation (Case 3, see Table 3), as well as conditions where the core rotates at a slower and faster speed than the disk (Cases 4 and 5, $\beta_\infty = 0.4$ and 1.3, respectively).

Figures 9(*a*)–9(*c*) show computed flow streamlines in the tangential $(\phi - z)$ plane at the receiver hole radius r_b in a frame of reference rotating at the speed of the rotor (in the left to right direction), for Cases 3–5, respectively. These streamlines were again determined by CFX [13]. In each image, the stator is at the

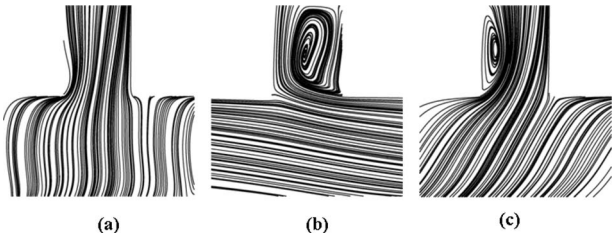

Fig. 9 Computed streamlines in the tangential plane at the receiver hole radius r_b: (*a*) Case 3, (*b*) Case 4, and (*c*) Case 5

bottom and the receiver hole and outlet is at the top.

For Case 4 (Fig. 9(*b*)), $\beta_\infty = 0.4$ and the flow is underswirled; the receiver hole rotates more quickly than the flow in the core, therefore, the flow enters at an acute angle, separating at the leading edge of the hole and causing a recirculation inside the hole. As the preswirl ratio is increased, the angle at which the flow enters the receiver hole tends toward the axial direction. At the point where synchronous rotation between the flow and the hole occurs, the flow would be expected to flow axially into the receiver hole, as can be seen in Fig. 9(*a*) (Case 3), for which $\beta_\infty = 1.0$. When the swirl ratio is increased further, or overswirled, the flow rotates more quickly than the receiver hole, causing separation and a region of recirculation at the trailing edge of the hole, as seen in Fig. 9(*c*) (Case 5). Note that Lewis et al. [13] showed that the discharge coefficient of the receiver holes is a maximum at synchronous rotation.

Figure 10(*a*) shows a contour map of the heat transfer coefficient on the rotating disk in isometric view for Case 3. The disk is shown rotating in the clockwise direction and the data is again determined from the 40°C narrow-band TLC. The fluid-dynamic conditions feature synchronous rotation, and the heat transfer, dominated by impingement on the rotating disk, is symmetric with respect to the receiver holes. Superimposed onto the figure are three computed streamlines of cooling air relative to the rotor (again determined by CFX). Some of the inlet flow enters the receiver holes directly (streamline A, orange), while the remaining flow (streamlines B and C, black) impinges upon the region between the holes. The impinging flow spreads both radially and circumferentially from the impingement region, some exiting through the receiver hole and some continuing to a higher radius where it recirculates into the system and mixes with the core flow.

Figure 10(*b*) illustrates the heat transfer contours for Case 4, where the flow is underswirled. Superimposed onto the contours are two streamlines of cooling air from the preswirl nozzles. Streamline A (orange) flows directly out through the receiver hole. Streamline B (black) has a less direct route, impinging onto the downstream side of the hole and forming part of a new boundary layer, eventually exiting through the next (anticlockwise) receiver hole; this impingement and the associated thin boundary layer gives rise to the crescent-shaped region of high heat transfer on the "downstream" side of each receiver hole.

Figure 10(*c*) illustrates the heat transfer contours for Case 5, where the flow is overswirled, with a corresponding translation of the crescent-shaped region of high heat transfer to the downstream side of the receiver holes.

Figure 11 is a plot of $\mathrm{Nu}\,\mathrm{Re}_\phi^{-0.5}$ along a circumferential line between the receiver holes at the receiver hole radius for fluid-dynamic conditions featuring a synchronous rotation at three rotational Reynolds numbers. This parameter is shown to be virtually independent of Re_ϕ, indicating that the heat transfer is governed by impingement.

6 Conclusions

In this paper, two narrow-band liquid crystals were used to measure the surface temperature on a rotating disk in a transient

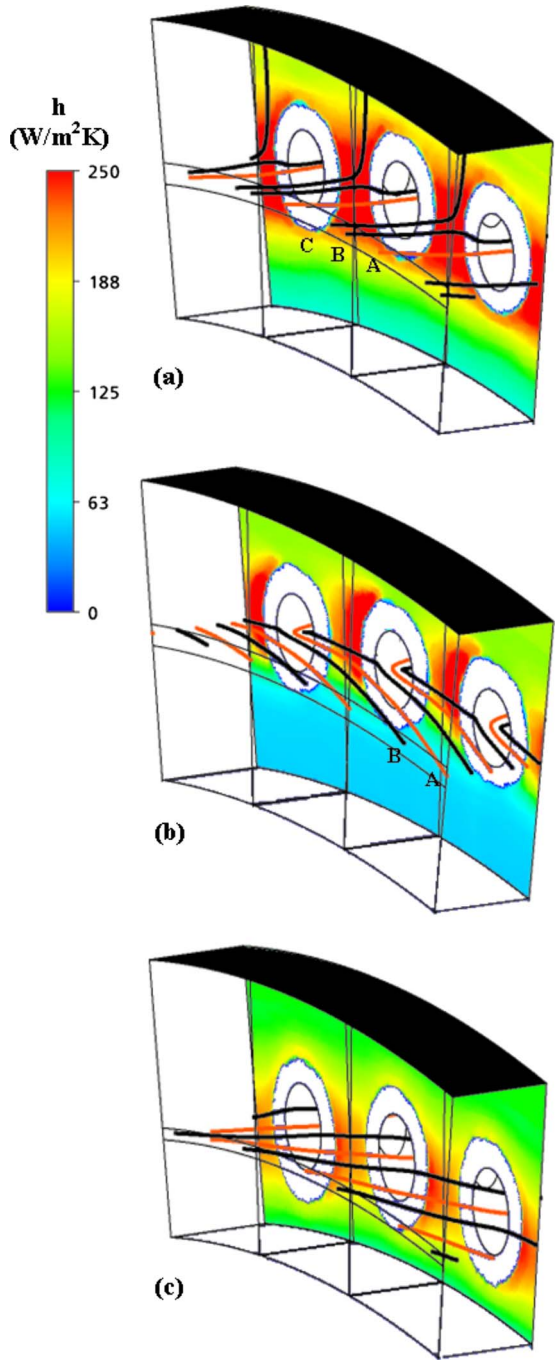

Fig. 10 Heat transfer coefficient in isometric view for high-radius preswirl system: (*a*) Case 3, (*b*) Case 4, and (*c*) Case 5

experiment, which models the flow of cooling air in a gas turbine. The convective heat transfer coefficient h was subsequently calculated from the solution of Fourier's conduction equation, accounting for the exponential rise in the air temperature driving the heat transfer. The relevant nondimensional parameters in the solution (Θ, λ, and β_τ) were sufficiently advantageous to produce relatively low uncertainties in the measured h for both crystals.

Low-radius and high-radius preswirl designs were investigated, with $r_p/r_b = 0.8$ and 1.0, respectively. For the low-radius design, the experiments revealed two heat transfer regimes: a *viscous* regime at relatively low coolant flow rates, where the fluid dynamics was governed by the turbulent boundary layer on the rotating disk; and an *inertial* regime at higher flow rates, where impingement effects were prominent. Both regimes featured regions of

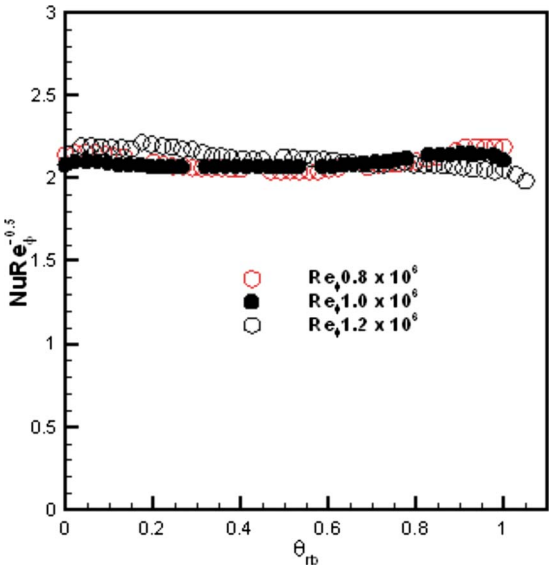

Fig. 11 Circumferential variation in Nu $Re_\phi^{-0.5}$ for high-radius preswirl system

high heat transfer where thin boundary layers replaced air exiting though holes at high radius on the rotating disk. The heat transfer in the high-radius preswirl system was shown to be dominated by impingement under the flow conditions tested. The Nusselt number on the disk was shown to scale with $Re_\phi^{0.8}$ and $Re_\phi^{0.5}$ in the viscous and inertial regimes, respectively.

The results presented here give insight into the heat transfer mechanisms in the preswirl flow and they also provide data for the validation of CFD codes and scaling relationships. The paper also illustrates the power of thermochromic liquid crystals for accurate heat transfer measurements in rotating systems.

Nomenclature

a, b = inner and outer radii of disk
c_w = nondimensional mass flow rate$=\dot{m}/\mu b$
c = specific heat
$f(\beta)$ = step-change solution of Fourier's equation
$g(\beta, \beta_\tau)$ = exponential solution of Fourier's equation
h = heat transfer coefficient
H = hue
k = conductivity
$\dot{m}$ = mass flow rate
Nu = Nusselt number
P_h = relative uncertainty in h
P_T = relative uncertainty in T
q_w = heat flux at the wall
Re_ϕ = rotational Reynolds number$=\rho\Omega b^2/\mu$
r = radius
s = rotor-stator separation distance
t = time
T = temperature
V = velocity
β = parameter, step-change solution$=h\sqrt{t/\rho ck}$
β_τ = parameter, exponential solution$=h\sqrt{\tau/\rho ck}$
β_∞ = swirl ratio $(=V_\phi/\Omega r)$ in the core
β_b = preswirl ratio based on r_b $(=V_{\phi,p}/\Omega r_b)$
β_p = preswirl ratio based on r_p $(=V_{\phi,p}/\Omega r_p)$
Φ_h^* = amplification parameter for uncertainty in h
λ = parameter, exponential solution$=\sqrt{t/\tau}$
λ_T = turbulent flow parameter$=c_w\,Re_\phi^{-0.8}$
μ = dynamic viscosity
ρ = density
Θ = nondimensional temperature
θ_{r_b} = circumferential angle at r_b
Ω = angular velocity of rotor

Subscripts

a = total, air
aw = adiabatic wall
b = blade-cooling
p = preswirl
w = wall
ϕ, r, z = circumferential, radial, and axial directions
0 = value at time zero
1,2,3 = terms in the exponential series
∞ = value in core, $z/s=0.5$, $r/r_b=1$; infinite time

References

[1] Scricca, J. A., and Moore, K. D., 1997, "Effects of 'Cooled' Cooling Air on Pre-Swirl Nozzle Design," Technical Report No. NASA/CP-98-208527.
[2] El-Oun, Z. B., and Owen, J. M., 1989, "Preswirl Blade Cooling Effectiveness in an Adiabatic Rotor-Stator System," ASME J. Turbomach., **111**, pp. 522–529.
[3] Chew, J. W., Ciampoli, F., Hills, N. J., and Scanlon, T., 2005, "Pre-Swirled Cooling Air Delivery System Performance," ASME Paper No. GT2005-68323.
[4] Farzaneh-Gord, M., Wilson, M., and Owen, J. M., 2005, "Numerical and Theoretical Study of Flow and Heat Transfer in a Pre-Swirl Rotor-Stator System," ASME Paper No. GT2005-68135.
[5] Meierhofer, B., and Franklin, C. J., 1981, "An Investigation of a Preswirled Cooling Airflow to a Turbine Disc by Measuring the Air Temperature in Rotating Channels," ASME Paper No. 81-GT-132.
[6] Wilson, M., Pilbrow, R., and Owen, J. M., 1997, "Flow and Heat Transfer in a Preswirl Rotor-Stator System," ASME J. Turbomach., **119**, pp. 364–373.
[7] Geis, T., Dittmann, M., and Dullenkopf, K., 2004, "Cooling Air Temperature Reduction in a Direct Transfer Preswirl System," ASME J. Eng. Gas Turbines Power, **126**, pp. 809–815.
[8] Dittmann, M., Dullenkopf, K., and Wittig, S., 2004, "Discharge Coefficients of Rotating Short Orifices With Radiused and Chamfered Inlets," ASME J. Eng. Gas Turbines Power, **126**, pp. 803–808.
[9] Yan, Y., Farzaneh-Gord, M., Lock, G. D., Wilson, M., and Owen, J. M., 2003, "Fluid Dynamics of a Pre-Swirl Rotor-Stator System," ASME J. Turbomach., **125**, pp. 641–647.
[10] Lewis, P., Wilson, M., Lock, G. D., and Owen, J. M., 2007, "Physical Interpretation of Flow and Heat Transfer in Preswirl Systems," ASME J. Eng. Gas Turbines Power, **129**, pp. 769–777.
[11] Dittmann, M., Geis, T., Schramm, V., Kim, S., and Wittig, S., 2002, "Discharge Coefficients of a Preswirl System in Secondary Air Systems," ASME J. Turbomach., **124**, pp. 119–124.
[12] Jarzombek, K., Dohmen, H. J., Benra, F.-K., and Schneider, O., 2006, "Flow Analysis in Gas Turbine Pre-Swirl Cooling Air Systems: Variation of Geometric Parameters," ASME Paper No. GT2006-90445.
[13] Lewis, P., Wilson, M., Lock, G. D., and Owen, J. M., 2008, "Effect of Radial Location of Nozzles on Performance of Pre-Swirl Systems," ASME Paper GT2008-50295.
[14] Lock, G. D., Yan, Y., Newton, P. J., Wilson, M., and Owen, M. J., 2005, "Heat Transfer Measurements Using Liquid Crystals in a Preswirl Rotating-Disk System," ASME J. Eng. Gas Turbines Power, **127**, pp. 375–382.
[15] Owen, J. M., and Rogers, R. H., 1995, *Flow and Heat Transfer in Rotating Disc Systems. Volume 2: Rotating Cavities*, Research Studies Press, Taunton, UK/Wiley, New York.
[16] Ireland, P. T., and Jones, T. V., 2000, "Liquid Crystal Measurements of Heat Transfer and Surface Shear Stress," Meas. Sci. Technol., **11**, pp. 969–986.
[17] Baughn, J. W., 1995, "Liquid Crystal Methods for Studying Turbulent Heat Transfer," Int. J. Heat Fluid Flow, **16**, pp. 365–375.
[18] Newton, P. J., Yan, Y., Stevens, N. E., Evatt, S. T., Lock, G. D., and Owen, J. M., 2003, "Transient Heat Transfer Measurements Using Thermochromic Liquid Crystal. Part 1: An Improved Technique," Int. J. Heat Fluid Flow, **24**, pp. 14–22.
[19] Kingsley-Rowe, J. R., Lock, G. D., and Owen, J. M., 2005, "Transient Heat Transfer Measurements Using Thermochromic Liquid Crystal: Lateral-Conduction Error," Int. J. Heat Fluid Flow, **26**, pp. 256–263.
[20] Owen, J. M., Newton, P. J., and Lock, G. D., 2003, "Transient Heat Transfer Measurements Using Thermochromic Liquid Crystal. Part 2: Experimental Uncertainties," Int. J. Heat Fluid Flow, **24**, pp. 23–28.
[21] Fang, C. J., Wu, M. C., Kuo, Y. M., Lee, C. Y., Peng, C. H., and Hung, Y. H., 2007, "Heat Transfer Behavior for a Stationary or Rotating MCM Disk With an Unconfined Round Jet Impingement," J. Electron. Packag., **129**, pp. 400–410.